

# Modeling and Correcting Cure-Through in Continuous Stereolithographic 3D Printing

Zachary D. Pritchard, Martin P. de Beer, Riley J. Whelan, Timothy F. Scott, and Mark A. Burns\*

Continuous stereolithography offers significant speed improvements over traditional layer-by-layer approaches but is more susceptible to cure-through, undesired curing along the axis of exposure. Typically, cure-through is mitigated at the cost of print speed by reducing penetration depth in the photopolymer resin via the addition of nonreactive light absorbers. Here, a mathematical approach is presented to model the dose profile in a part produced using continuous stereolithography. From this model, a correction method is developed to modify the projected images and produce a chosen dose profile, thereby reducing cure-through while maintaining print speed. The method is verified experimentally on a continuous stereolithographic 3D printer, and the practicality of various dose profiles is investigated. In optimizing the critical dose parameter, the measured gelation dose  $D_{\text{gel}}$  is found to be insufficient for accurate reproduction of features, and an optimal value of  $D_c = 5D_{\text{gel}}$  is chosen for the test resin. Using optimized parameters with a high-absorbance height resin ( $h_a = 2000 \mu\text{m}$ ), feature height errors are reduced by over 85% in a test model while maintaining a high print speed ( $s = 750 \text{ mm h}^{-1}$ ).

Additive manufacturing (AM), commonly called 3D printing, refers to a number of technologies through which objects are created by progressive addition of material.<sup>[1,2]</sup> With its simplicity and nearly unlimited design choice, AM is attractive for producing custom, limited-quantity, and prototype parts. AM has found numerous applications in fields including biomedical engineering,<sup>[3–7]</sup> bioinspired materials,<sup>[8–10]</sup> functional materials,<sup>[11–17]</sup> and the DIY “maker” industry.<sup>[18]</sup> In projection stereolithography, a widely used AM method, photopolymerizable resin is exposed to patterned light to cure cross-sections of

a desired 3D part. Typically, stereolithography produces parts in discrete layers. Exposed areas are cured through the full layer height, whereupon the part is repositioned and recoated with resin before the next layer is exposed. Recently, *continuous* stereolithographic technologies have been developed which increase print speeds by eliminating the time-consuming repositioning and recoating steps.<sup>[19,20]</sup> Print speed in continuous stereolithography is dependent on the resin absorbance height, with low-absorbance resins allowing extremely high print speeds of up to  $2000 \text{ mm h}^{-1}$  at the cost of part fidelity.<sup>[20]</sup>

In stereolithography, the penetration depth of light in the resin limits accuracy along the vertical axis: unaccounted-for light propagation can cause undesired curing, known as *cure-through*, *over-cure*,<sup>[21,22]</sup> the *back-side effect*,<sup>[23]</sup> or *print-through error*.<sup>[19,24]</sup> This phenomenon can

also contribute to cross-linking heterogeneity, introducing internal stresses which can deform the part and further reduce fidelity.<sup>[25]</sup> The prevalent strategy to mitigate cure-through is to add nonreactive light absorbers to the resin formulation.<sup>[21,25–28]</sup> Highly absorbing resins have been widely adopted despite the slower print speeds needed to ensure fully cured layers. Alternatively, cure-through can be mitigated without sacrificing speed by modifying the projected images, known as *slices*, based on modeling of the curing process. Optimization-based methods to eliminate cure-through by adjusting model dimensions have been developed for external surfaces and internal voids in traditional stereolithography.<sup>[22,24,29]</sup> Manual adjustments to account for cure-through have also been reported.<sup>[30]</sup>

Nevertheless, slice correction has not been described for continuous stereolithography, where cure-through is a more significant and complex problem. Furthermore, existing models of continuous stereolithography are not tailored to this application.<sup>[31–33]</sup>


Here, we present a curing model and a slice correction algorithm for continuous stereolithography. Previous noncontinuous approaches used iterative and heuristic processes to find optimal corrections and were restricted to black and white pixels; our correction method uses grayscale, which has previously only been used to improve lateral resolution,<sup>[34]</sup> along with an exact mathematical solution to precisely set the dose profile within a part. We also present experimental validation of our model and correction approach using a recently developed two-color continuous stereolithographic 3D printer.<sup>[20]</sup> These methods are

Z. D. Pritchard, M. P. de Beer, R. J. Whelan, Prof. T. F. Scott, Prof. M. A. Burns

Department of Chemical Engineering  
University of Michigan  
Ann Arbor, MI 48109, USA  
E-mail: maburns@umich.edu

Prof. T. F. Scott  
Department of Chemical Engineering  
Monash University  
Clayton, VIC 3800, Australia

Prof. T. F. Scott  
Department of Materials Science and Engineering  
Monash University  
Clayton, VIC 3800, Australia

 The ORCID identification number(s) for the author(s) of this article can be found under <https://doi.org/10.1002/admt.201900700>.

DOI: 10.1002/admt.201900700

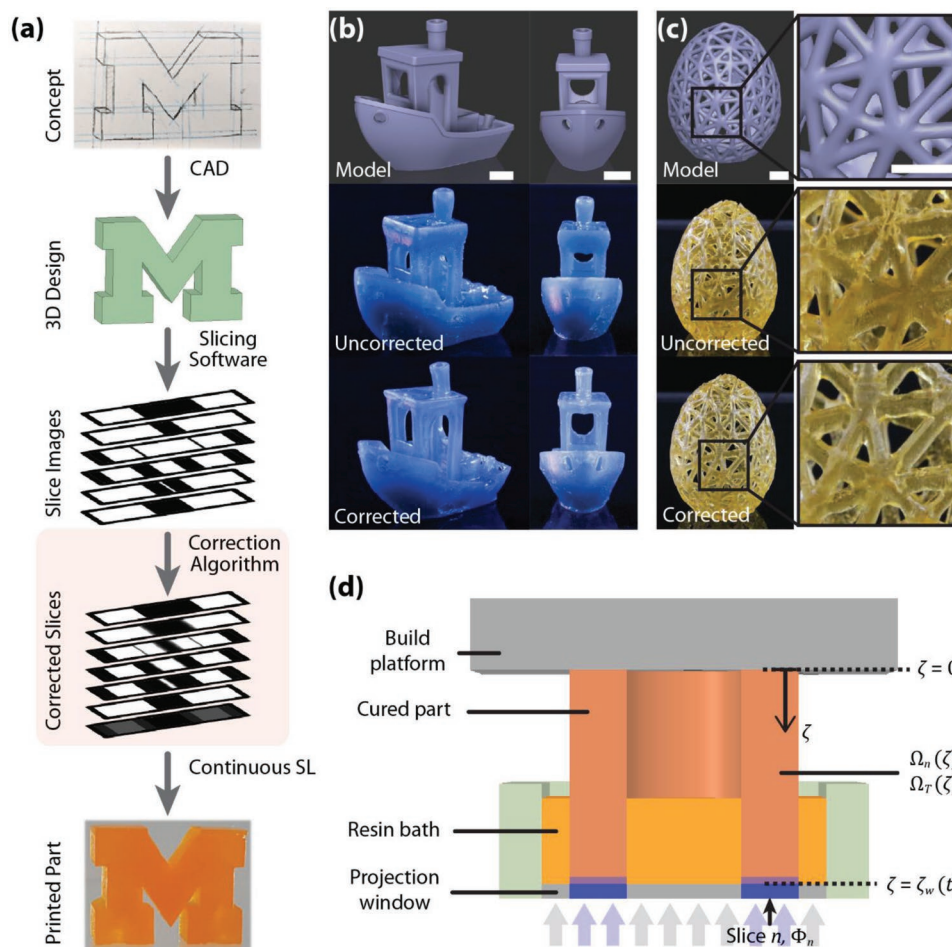


**Figure 1.** a) Cure-through correction is incorporated into the 3D printing workflow by computationally processing slice images. b,c) Correction applied to real models, reducing the extent of cure-through while maintaining print speed. Scale bars are 5 mm. b) #3DBenchy<sup>[35]</sup> printed at  $800 \text{ mm h}^{-1}$  ( $h_a = 1500 \text{ } \mu\text{m}$ ,  $D_c = 230 \text{ mJ cm}^{-3}$ ), and c) hollow egg<sup>[36]</sup> printed at  $800 \text{ mm h}^{-1}$  ( $h_a = 2000 \text{ } \mu\text{m}$ ,  $D_c = 173 \text{ mJ cm}^{-3}$ ). d) Vertical cross-section of printer setup showing nondimensionalized variables of interest:  $\zeta$ ,  $\Omega_n$ , and  $\Phi_n$  are the dimensionless z-position, dose, and light intensity, respectively.

adapted for traditional layer-by-layer stereolithography in Section S6 (Supporting Information).

Figure 1 shows how our correction process fits into the existing 3D printing workflow. To demonstrate the applicability of the slice correction method to typical parts, we printed corrected and uncorrected versions of two open-source models (Figure 1b,c).<sup>[35,36]</sup> In both cases, parts printed with uncorrected slices significantly deviate from the design as a result of cure-through. Applying slice correction to these parts significantly reduces the occurrence of cure-through, with corrected parts showing improved accuracy in the z-direction. Video S1 in the Supporting Information demonstrates real-time printing of uncorrected and corrected parts.

A schematic of the printer and coordinate system is shown in Figure 1d. The coordinate system is defined with respect to the build platform, with  $z = 0$  at the platform and increasing toward the projection window (i.e., downward). The coordinates  $x$  and  $y$  are omitted from our notation for simplicity; however, the presented equations must be applied at fixed ( $x$ ,  $y$ ) positions since the projected slices are patterned. The build platform begins in contact with the window and continuously

moves upward while printing. The curing model, then, includes simultaneous continuous and discrete processes: as the build platform continuously ascends, exposure patterns change at discrete intervals with each slice projected in sequence. Below, we present a brief description of the model; a complete derivation is available in Section S2 (Supporting Information).

To account for the discrete projection of slices, the total accumulated dose at a point is a sum of contributions from each slice projected.  $D_T(z)$  is the total volumetric dose delivered to position  $z$  in the final part, and the contribution of slice  $n$  to the total dose is  $D_n(z)$ . Thus,  $D_T(z) = \sum_{n=0}^N D_n(z)$  where slices are numbered from zero to  $N$  in order of exposure. From Beer's Law, the time-derivative of volumetric dose as a slice is projected is

$$\frac{d}{dt} D_n(z, t) = \frac{\ln 10}{h_a} I_{n,w} 10^{-[z_w(t)-z]h_a^{-1}} \quad (1)$$

where  $I_{n,w}$  is the light intensity at the window,  $z_w(t)$  is the time-varying position of the window, and  $h_a$  is the resin absorbance

height (i.e., the propagation distance over which the intensity falls to 10% of its initial value).

With the build platform continuously ascending,  $D_n(z)$  is determined for each slice by integrating over the time period when the slice is projected. Since the coordinate system is fixed with respect to the build platform, time-dependence can be incorporated via the continuously increasing value of  $z_w(t)$  and the print speed  $s = dz_w/dt$ . Integrating Equation (1) over the exposure of slice  $n$  yields Equation (2)

$$D_n(z) = \frac{I_{n,w}}{s} \left\{ 10^{-(nh_s - z)/h_s} - 10^{-[(n+1)h_s - z]/h_s} \right\} \quad (2)$$

where  $h_s$  is the slicing height. Equation (2) applies if the cross-section at height  $z$  is exposed to slice  $n$  (i.e., when  $z \leq nh_s$ ); otherwise,  $D_n(z) = 0$ . The total accumulated dose at a point,  $D_T(z)$ , is obtained by summing Equation (2) over all slices to which  $z$  is exposed

$$D_T(z) = \sum_{n=z/h_s}^N \frac{I_{n,w}}{s} \left\{ 10^{-(nh_s - z)/h_s} - 10^{-[(n+1)h_s - z]/h_s} \right\} \quad (3)$$

or, in dimensionless form

$$\Omega_T(\zeta) = \sum_{n=\zeta}^N \Phi_n \left\{ 10^{-(n-\zeta)\eta} - 10^{-[(n+1)-\zeta]\eta} \right\} \quad (4)$$

with dimensionless variables  $\Omega \equiv DD_c^{-1}$  (where  $D_c$  is the experimentally determined critical dose),  $\zeta \equiv zh_s^{-1}$ ,  $\Phi \equiv I_w I_c^{-1}$  (where  $I_c$  is the minimum intensity needed to reach  $D_c$ ), and  $\eta \equiv h_s h_a^{-1}$ . Equation (4) allows calculation of  $\Omega_T$  for any integer value of  $\zeta$  in the final printed part.

Equation (4) can be simplified to quickly perform dose calculations and slice corrections by writing  $\Omega_T(\zeta)$  as a function of  $\Omega_T(\zeta + 1)$

$$\Omega_T(\zeta) = \Phi_\zeta (1 - 10^{-\eta}) + \Omega_T(\zeta + 1) 10^{-\eta} \quad (5)$$

Starting at the bottom of the part (i.e.,  $\zeta = N$ ) and moving upward, the total dose may be calculated for each integer value of  $\zeta$  by considering only the current layer and the preceding layer. Expressions for  $\Omega_T$  at several values of  $\zeta$ , along with a full derivation, are available in Section S2 (Supporting Information).

The above mathematical model allows calculation of the accumulated optical dose at any position in the part and any time in the printing process. Since  $D_c$  defines the threshold for curing, an accurate dose profile has  $\Omega_T \geq 1$  within designed features and  $\Omega_T < 1$  outside features. At points where these conditions are not met, the printed part will exhibit undercure or cure-through artifacts.

Figure 2 shows modeled results for a ladder-like part printed using the default slicing approach, in which the maximum intensity is projected whenever an intended feature is adjacent to the window. There is significant cure-through into the gaps, and the bottom of the second feature is undercured. Rather than producing the desired two features, the conventional approach yields a single, large feature.

The total dose profile shown in Figure 2d is the result of contributions from all slices projected, as expressed in Equation (4).

A closer look at the bottom feature highlights the causes of cure-through and undercure: Figure 2e shows the contribution of each slice to the total dose for this feature and, thus, the evolution of the dose curve during the continuous printing process. The uncorrected slices use only the maximum and minimum projector intensities ( $p = 1$  and  $p = 0$ , respectively). While the maximum intensity is projected ( $n = 31$ – $40$ ), the accumulated dose rapidly increases for all  $\zeta \leq n$ . The nonzero minimum intensity results from light scatter in the projection system and is related to the projector contrast ratio (see Section S3, Supporting Information). Dose contributions while the minimum intensity is projected ( $n = 21$ – $30$  and  $n = 41$ – $50$ ) are relatively small. In the gap from  $\zeta = 21$  to  $30$ , the small contributions from minimum-intensity slices are overwhelmed by the contributions from maximum-intensity slices, resulting in cure-through. The feature is correctly cured from  $\zeta = 31$  to approximately  $38$  then undercured through its designed bottom edge at  $\zeta = 41$ , highlighting that a point must be exposed over several slices to fully cure—even when projecting the maximum intensity. Finally, the gap below the feature correctly remains uncured. From this simple example, it is apparent that cure-through and undercure are inevitable when using unmodified slices with low-absorbance resins. This analysis also suggests that carefully designed slice images could achieve the desired geometry.

The primary requirement for correcting cure-through and undercure is that the full height of each feature is cured without gelling nonfeatures. However, as has been recently discussed with respect to tomographic printing, it is not possible to deliver exactly the critical dose within features and exactly zero dose outside features: to do so requires the ability to effectively “subtract” dose using negative intensities.<sup>[37]</sup> Clearly, not all dose profiles are achievable. Physically attainable dose profiles must be continuous and are limited by resin properties and printing parameters. These considerations define a set of three constraints, illustrated in Figure 3 and derived in Section S4 (Supporting Information):

- (i) For all points within a feature,  $\Omega_T \geq 1$ ; for all other points,  $\Omega_T < 1$ . Since  $\Omega_T$  varies continuously with  $\zeta$ , features will only be reproduced accurately if  $\Omega_T = 1$  along edges.
- (ii) The maximum projector intensity, print speed, and resin absorbance height determine the maximum rate at which the dose can increase. With  $\Omega_T = 1$  fixed at the bottom edge of the feature, these parameters define a maximum dose within the feature and a minimum dose below the feature.
- (iii) From Equation (4), the minimum dose at point  $\zeta$  is limited by the minimum projector intensity, the print speed, the resin absorbance height, and the dose at point  $\zeta + 1$ . With the dose at the top edge set at the critical dose, these parameters define a maximum dose within the feature and a minimum dose above the feature.

If any of these constraints are violated, the feature’s edges will shift from their designed positions.

The three constraints define *target dose regions*, indicated by shading in Figure 3a. These regions are demonstrated here for a particular feature, but they can be generated for any feature height by shifting curves (ii) and (iii) along the  $\zeta$ -axis such that the edges of the feature remain at the critical dose. Since the

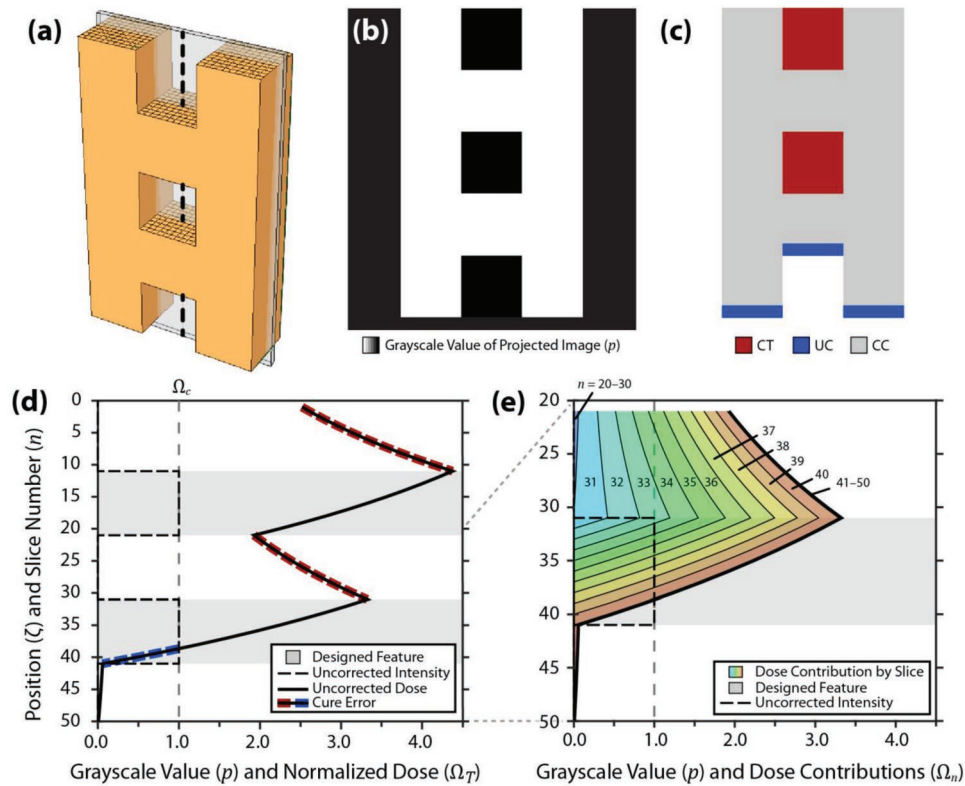


**Figure 2.** a) Test model. b) Vertical stack of uncorrected grayscale projections along the plane indicated in (a). Note that only black and white ( $p = 0$  and  $p = 1$ ) are used by default. c) Model prediction from slices in (b) showing areas with cure-through (CT, red) and undercuring (UC, blue). Gray regions of the part are correctly cured (CC). d) Grayscale value as a function of  $n$  and total accumulated dose as a function of  $\zeta$  for the  $(x,y)$  position indicated by the dashed line in (a).  $D_c = 576 \text{ mJ cm}^{-3}$ ,  $h_s = 50 \text{ }\mu\text{m}$ ,  $h_a = 2000 \text{ }\mu\text{m}$ , and  $s = 1000 \text{ mm h}^{-1}$ .  $\zeta = 0$  corresponds to the top of the part (i.e., the surface attached to the build platform). The grayscale value  $p$  relates to the intensity of the projected pixel when  $\zeta_w = n$  (calibration curve available in Figure S1, Supporting Information). Shaded areas indicate designed features. The dose curve indicates the normalized total dose  $\Omega_T$  at position  $\zeta$  on completion of the print, with cure errors indicated in red (cure-through) or blue (undercure). e) Evolution of the total dose curve shown in (d) for  $n = 21$  to  $n = 50$ . The total dose is the sum of contributions from individual slices, each labeled and represented by a color.

doses at adjacent points are interrelated, it is not possible to generate arbitrary dose profiles within the regions. However, there are an infinite number of achievable profiles which fall entirely within the target dose regions and thus produce an accurate part.

To implement slice correction, a valid dose profile is determined for the feature, and Equation (5) is solved for each pixel of each slice (starting from the bottom of the part) to determine the intensity required to reach the desired dose. One approach

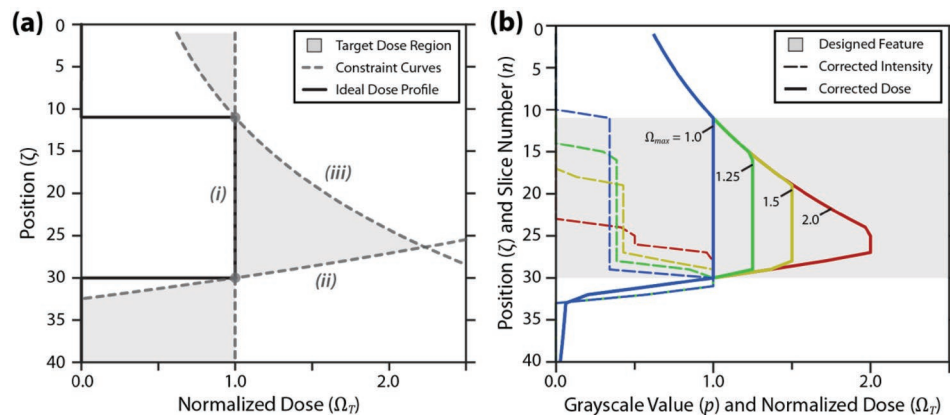


**Figure 3.** a) Three constraints which define the target dose region (shaded): (i) curing of features while nonfeatures remain uncured, (ii) exposure at the maximum dose at the bottom of the feature, and (iii) exposure at the minimum dose at the top of the feature. b) Valid dose profiles defined by maximum dose  $\Omega_{\max}$  with corresponding intensity profiles. Here, shading indicates the designed feature height. For a given set of parameters, the intensity profile can be tailored to achieve either a uniform dose or a high peak dose within features while still eliminating cure errors.



to designing dose profiles is in terms of a *maximum dose*,  $\Omega_{\max}$ . Constraint curves (ii) and (iii) are traced up to the prescribed  $\Omega_{\max}$ , which is maintained within the center of the feature. Figure 3b shows a collection of these dose profiles and the intensities needed to achieve them.

For the important case of  $\Omega_{\max} = 1$ , the critical dose is uniformly delivered throughout the feature. We applied this correction to the model in Figure 2a, with results illustrated in **Figure 4**. A comparison of Figures 4a and 2b shows how the correction process modifies slices. For the rung-like inner features, the intensity is reduced through most of the feature and a high-intensity burst is delivered at the bottom. Since there is no possibility of cure-through for the outer features, they are exposed at the maximum intensity. Figure 4b indicates that the correction has completely eliminated cure-through and undercure in our modeled result. Figure 4c,d shows how the corrected slices achieve the desired dose profile. The high intensity burst at the bottom of the feature ensures all layers reach the critical dose. From the bottom-up perspective of the correction calculations, a constant intensity maintains the dose from one layer to the next after the critical dose is achieved at the bottom of the feature. From Equation (5), the intensity required to maintain a dose between two layers is  $\Phi_n = \Omega_T$ . Thus, to maintain the critical dose  $\Phi_n = \Omega_c = 1$ .

To achieve higher maximum doses, features must be exposed at higher intensities for shorter periods, as shown in Figure 3b; a smaller fraction of the feature is exposed so that constraint (iii) is not violated. Though the edges of the feature are at the critical dose for each intensity profile, the interior dose varies considerably. As a result, it is important to optimize  $\Omega_{\max}$  as well as  $D_c$  to ensure good part quality: high doses drive additional cross-linking, improving the part's green strength (i.e., its tensile strength before postprocessing) to ensure a rigid and printable structure but also introducing heterogeneous internal stresses that can deform the part. Conversely, low doses with long exposure times might not sufficiently cure the part since flow is not perfectly uniaxial and the resin bath is not infinitely deep. The optimal correction parameters depend in some degree on the irradiation system, the geometry of the part, the flow profile in the resin bath, and the chemical and mechanical properties of the resin.

To test the correction algorithm and optimize its parameters, low-absorbance photopolymer resins were prepared (Table S1, Supporting Information) for use with a previously described two-color continuous stereolithographic 3D printer.<sup>[20]</sup> Experimental results are shown in **Figure 5**. The absorbance height  $h_a$  and gelation dose  $D_{\text{gel}}$  were determined from the resin working curves (Figure 5a, and Section S1.3, Supporting Information), and the test geometry in Figure 5b was used to investigate the effect of the critical dose parameter on print fidelity. We printed test parts using several values of  $D_c$  and an unconstrained maximum dose ( $\Omega_{\max} = \infty$ ), with results shown in Figure 5b–d. Supplying exactly the measured gelation dose (i.e.,  $D_c = D_{\text{gel}}$ ) results in missing features and poor fidelity; feature sizes increase as  $D_c$  increases, and at higher values of  $D_c$  cure-through is observed (Figure 5c). As discussed above, a critical dose higher than the gelation dose is likely required due to the simplifying assumptions used in the correction algorithm and the need for a part of sufficient green strength. For the geometry, resin, and print conditions considered,  $D_c = 5D_{\text{gel}} = 748 \text{ mJ cm}^{-3}$  is the optimal critical dose, achieving

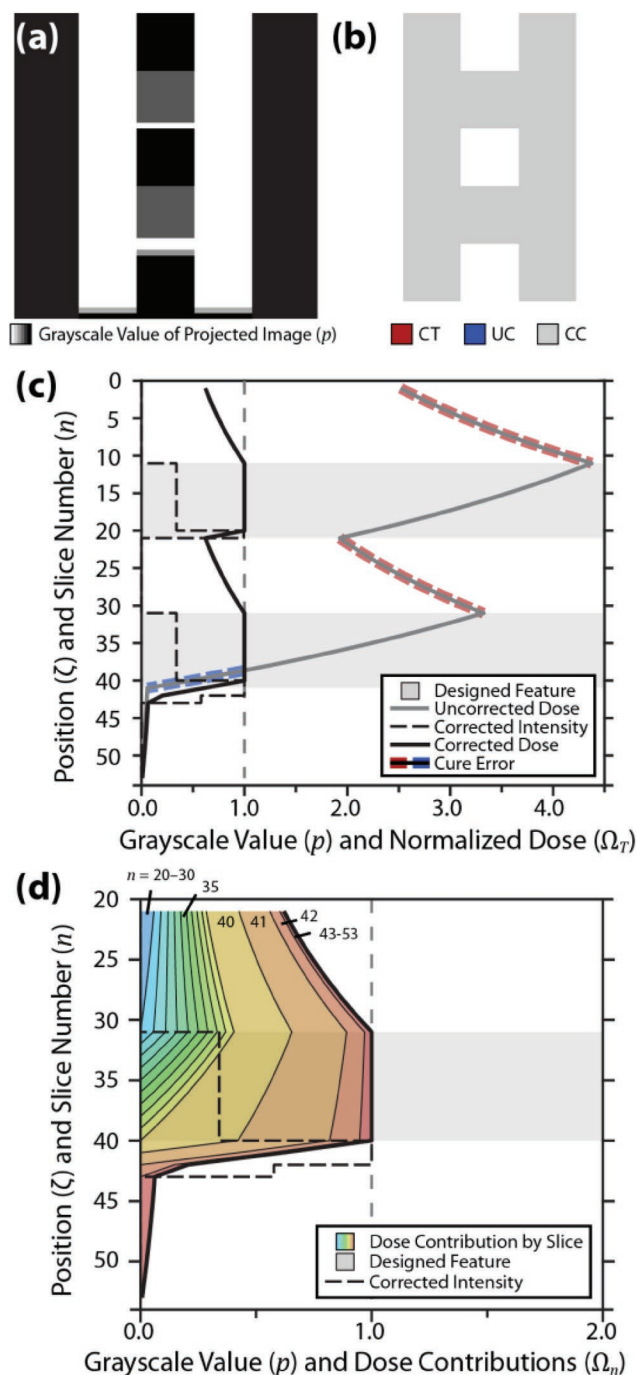


**Figure 4.** Correction for model in Figure 2a with  $\Omega_{\max} = 1$ . a) Vertical stack of corrected grayscale projections along the plane indicated in Figure 2a. b) Model prediction from slices in (a) showing no cure-through (CT, red) or undercure (UC, blue). The full part is correctly cured (CC, gray). c) Corrected grayscale value and dose for the  $(x, y)$  position indicated by the dashed line in Figure 2a. Note that the correction process required additional slices beyond the original 50 to ensure the bottom of the part was fully cured.  $D_c = 576 \text{ mJ cm}^{-3}$ ,  $h_s = 50 \text{ }\mu\text{m}$ ,  $h_a = 2000 \text{ }\mu\text{m}$ , and  $s = 1000 \text{ mm h}^{-1}$ . d) Contributions of individual slices to the accumulated dose curve shown in (c) for  $n = 21$  to  $n = 53$ .

a marked improvement in fidelity without reducing print speed (Figure 5b). Additional optimization details are available in Section S5 (Supporting Information).

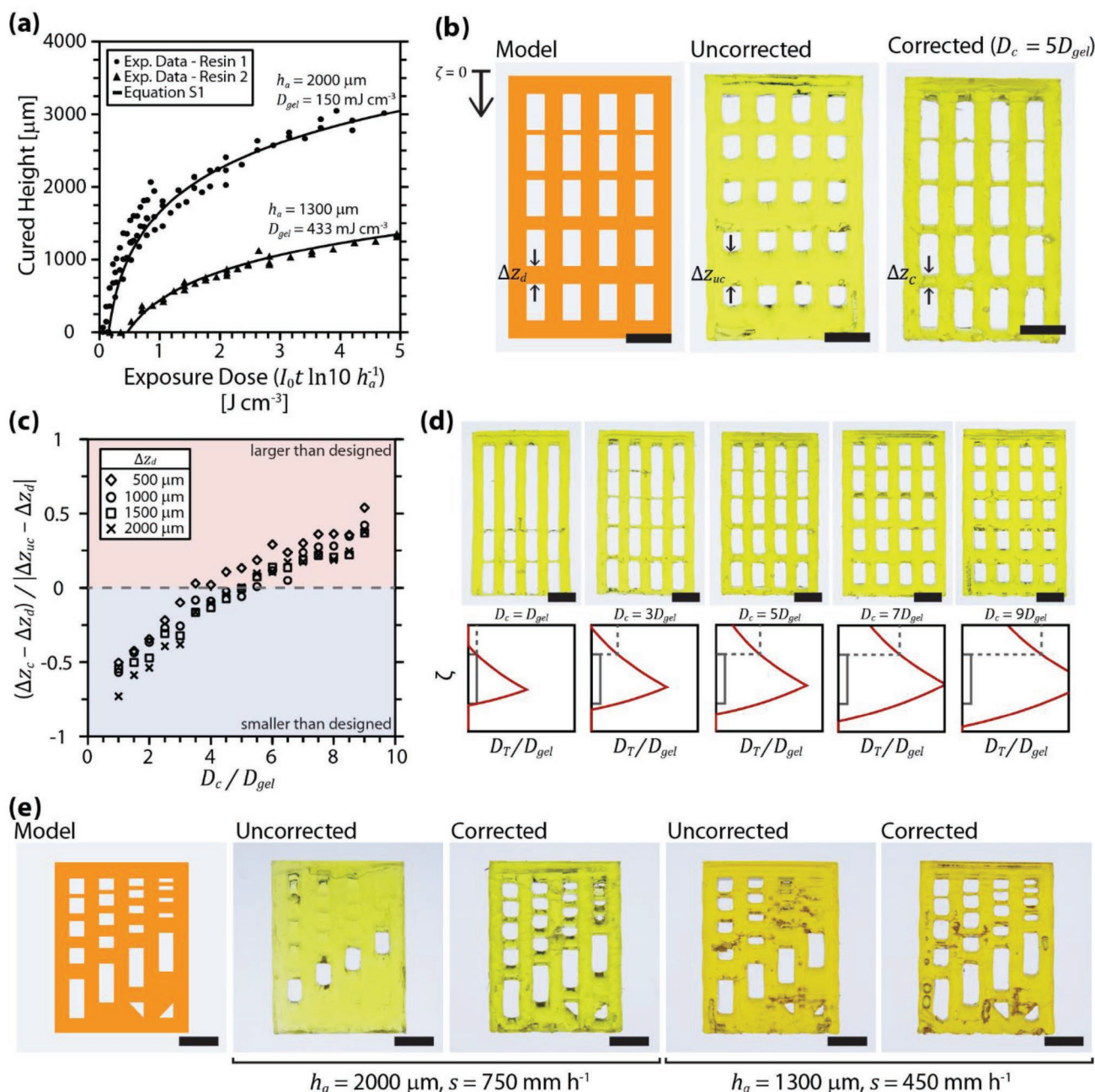


**Figure 5.** a) Cured thickness versus exposure dose of blue light for two acrylate-based resins (see Table S1, Supporting Information) with differing concentrations of blue light absorber. b) Test model (left), uncorrected test part (center), and corrected test part printed with  $D_c = 5 D_{gel} = 748 \text{ mJ cm}^{-3}$  (right). Parts printed in Resin 1 at  $750 \text{ mm h}^{-1}$ . c) Ratio of height errors (corrected-to-uncorrected) for a range of feature sizes and values of  $D_c$ . A ratio of zero corresponds to a perfectly corrected feature. d) Parts printed at  $750 \text{ mm h}^{-1}$  using slices corrected with different values for  $D_c$ . e) Corrected and uncorrected test parts for two resins with different absorber loadings (i.e.,  $h_a$ ) and print speeds. All scale bars are 10 mm.

To further improve fidelity, the traditional approach of adding dyes or pigments to reduce light propagation can be used in conjunction with slice correction (Figure 5e). As previously reported, the addition of dyes necessitates slower print speeds.<sup>[19,20]</sup> Regardless, applying slice correction at any dye loading or print speed improves the resolution, with higher dye loadings enabling printing of small features with less cure-through.

In summary, we have demonstrated a method for improving print fidelity on a two-color continuous stereolithographic

3D printer using resins with moderate to high absorbance heights. The approach analyzes and modifies the slice images for a model, using grayscale to precisely tune the dose profile throughout the final printed part. Furthermore, this approach allows control over the dose delivered within features, enabling continuous 3D printing of parts with dose-dependent functionality.<sup>[38]</sup> Though not demonstrated here, this technique is applicable to other continuous stereolithographic technologies, such as CLIP; these methods could also be applied to

noncontinuous stereolithography, as outlined in Section S6 (Supporting Information). Practically, this approach is limited by the resin green strength and the fluid dynamics of resin flow. Models that consider these effects or that vary critical dose with feature height might further improve fidelity. Nevertheless, this approach has afforded significant improvement in print quality for our system while maintaining high print speeds. Slice correction opens the door for the use of less-absorbing resins in stereolithographic systems, enabling faster print speeds and expanding the range of applications for additive manufacturing.

## Experimental Section

Experimental materials and methods can be found in Section S1 (Supporting Information).

## Supporting Information

Supporting Information is available from the Wiley Online Library or from the author.

## Acknowledgements

Z.D.P. and M.P.d.B. contributed equally to this work. This work was supported by the Michigan Translational Research and Commercialization (MTRAC) Innovation Hub for Advanced Transportation Kickstart program, the T.C. Chang Professorship (M.A.B.), and the University of Michigan Rackham Graduate Student Research Grant (Z.D.P. and M.P.d.B.).

## Conflict of Interest

T.F.S. and M.A.B. have an equity stake in Diplodocus, Inc., a developer of two-color continuous stereolithography equipment. The methods detailed in this work are the subject of a pending U.S. patent application.

## Keywords

3d printing, additive manufacturing, photopolymers, stereolithography

Received: August 15, 2019

Revised: September 30, 2019

Published online: October 21, 2019

- [1] T. D. Ngo, A. Kashani, G. Imbalzano, K. T. Q. Nguyen, D. Hui, *Composites, Part B* **2018**, *143*, 172.
- [2] O. Oderinde, F. Yao, H. Imtiaz, K. Li, M. Kang, G. Fu, S. Liu, *Polym. Adv. Technol.* **2018**, *29*, 1586.
- [3] R. D. Pedde, B. Mirani, A. Navaei, T. Styan, S. Wong, M. Mehrli, A. Thakur, N. K. Mohtaram, A. Bayati, A. Dolatshahi-Pirouz, M. Nikkhah, S. M. Willerth, M. Akbari, *Adv. Mater.* **2017**, *29*, 1606061.
- [4] A. K. Gaharwar, L. M. Cross, C. W. Peak, K. Gold, J. K. Carrow, A. Brokesh, K. A. Singh, *Adv. Mater.* **2019**, *31*, 1900332.
- [5] K. Kim, B. Kim, C. H. Lee, *Adv. Mater.* **2019**, <https://doi.org/10.1002/adma.201902051>.
- [6] P. Cai, Z. Li, E. S. Keneth, L. Wang, C. Wan, Y. Jiang, B. Hu, Y. Wu, S. Wang, C. T. Lim, E. V. Makeyev, S. Magdassi, X. Chen, *Adv. Mater.* **2019**, *31*, 1900514.
- [7] D. Shahriari, G. Loke, I. Tafel, S. Park, P. Chiang, Y. Fink, P. Anikeeva, *Adv. Mater.* **2019**, *31*, 1902021.
- [8] Y. Yang, X. Song, X. Li, Z. Chen, C. Zhou, Q. Zhou, Y. Chen, *Adv. Mater.* **2018**, *30*, 1706539.
- [9] A. Velasco-Hogan, J. Xu, M. A. Meyers, *Adv. Mater.* **2018**, *30*, 1800940.
- [10] G. Etienne, I. L. H. Ong, E. Amstad, *Adv. Mater.* **2019**, *31*, 1808233.
- [11] R. D. Farahani, M. Dubé, D. Therriault, *Adv. Mater.* **2016**, *28*, 5794.
- [12] L. Hirt, A. Reiser, R. Spolenak, T. Zambelli, *Adv. Mater.* **2017**, *29*, 1604211.
- [13] D. Cao, Y. Xing, K. Tantratian, X. Wang, Y. Ma, A. Mukhopadhyay, Z. Cheng, Q. Zhang, Y. Jiao, L. Chen, H. Zhu, *Adv. Mater.* **2019**, *31*, 1807313.
- [14] H. Wang, J. Shen, D. J. Kline, N. Eckman, N. R. Agrawal, T. Wu, P. Wang, M. R. Zachariah, *Adv. Mater.* **2019**, *31*, 1806575.
- [15] D. W. Yee, M. L. Lifson, B. W. Edwards, J. R. Greer, *Adv. Mater.* **2019**, *31*, 1901345.
- [16] W. Yang, J. Yang, J. J. Byun, F. P. Moissinac, J. Xu, S. J. Haigh, M. Domingos, M. A. Bissett, R. A. W. Dryfe, S. Barg, *Adv. Mater.* **2019**, *31*, 1902725.
- [17] N. Kleger, M. Cihova, K. Masania, A. R. Studart, J. F. Löffler, *Adv. Mater.* **2019**, *31*, 1903783.
- [18] M. Ratto, R. Ree, *First Monday* **2012**, *17*, <https://doi.org/10.5210/fm.v17i7.3968>.
- [19] J. R. Tumbleston, D. Shirvanyants, N. Ermoshkin, R. Januszewicz, A. R. Johnson, D. Kelly, K. Chen, R. Pinschmidt, J. P. Rolland, A. Ermoshkin, E. T. Samulski, J. M. DeSimone, *Science* **2015**, *347*, 1349.
- [20] M. P. de Beer, H. L. van der Laan, M. A. Cole, R. J. Whelan, M. A. Burns, T. F. Scott, *Sci. Adv.* **2019**, *5*, eaau8723.
- [21] J. Choi, R. B. Wicker, S.-H. Cho, C.-S. Ha, S. Lee, *Rapid Prototyping J.* **2009**, *15*, 59.
- [22] P. F. O'Neill, N. Kent, D. Brabazon, *AIP Conf. Proc.* **2017**, *1896*, 200012.
- [23] A. I. Shallan, P. Smejkal, M. Corban, R. M. Guijt, M. C. Breadmore, *Anal. Chem.* **2014**, *86*, 3124.
- [24] A. S. Limaye, D. W. Rosen, *Rapid Prototyping J.* **2006**, *12*, 283.
- [25] H. Gong, M. Beauchamp, S. Perry, A. T. Woolley, G. P. Nordin, *RSC Adv.* **2015**, *5*, 3627.
- [26] S. Zissi, A. Bertsch, J. Y. Jézéquel, S. Corbel, D. J. Lougnot, J. C. André, *Microsyst. Technol.* **1995**, *2*, 97.
- [27] C. Sun, X. Zhang, *J. Appl. Phys.* **2002**, *92*, 4796.
- [28] H. Gong, B. P. Bickham, A. T. Woolley, G. P. Nordin, *Lab Chip* **2017**, *17*, 2899.
- [29] A. S. Limaye, D. W. Rosen, *Rapid Prototyping J.* **2007**, *13*, 76.
- [30] M. J. Männel, L. Selzer, R. Bernhardt, J. Thiele, *Adv. Mater. Technol.* **2019**, *4*, 1800408.
- [31] D. Dendukuri, P. Panda, R. Haghgooie, J. M. Kim, T. A. Hatton, P. S. Doyle, *Macromolecules* **2008**, *41*, 8547.
- [32] Z. Wang, H. Liang, A. V. Dobrynin, *Macromolecules* **2017**, *50*, 7794.
- [33] S. Sarkar, S. Lin-Gibson, *Adv. Theory Simul.* **2018**, *1*, 1800028.
- [34] C. Zhou, Y. Chen, R. A. Waltz, *J. Manuf. Sci. Eng.* **2009**, *131*, 061004.
- [35] Creative Tools Sweden AB, “#3DBenchy – The jolly 3D printing torture-test,” <http://www.3dbenchy.com/>, n.d.
- [36] A. Nosek, “Easter Eggs by Antonin\_Nosek – Thingiverse,” <https://www.thingiverse.com/thing:2829553>, n.d.
- [37] B. E. Kelly, I. Bhattacharya, H. Heidari, M. Shusteff, C. M. Spadaccini, *Science* **2019**, *363*, 1075.
- [38] G. I. Peterson, J. J. Schwartz, D. Zhang, B. M. Weiss, M. A. Ganter, D. W. Storti, A. J. Boydston, *ACS Appl. Mater. Interfaces* **2016**, *8*, 29037.